

Ophiuchus: an optical view of a very massive cluster of galaxies hidden behind the Milky Way [★]

F. Durret¹, K. Wakamatsu², T. Nagayama³, C. Adami⁴, and A. Biviano^{5,1}

¹ Sorbonne Universités, UPMC Univ. Paris 6 et CNRS, UMR 7095, Institut d'Astrophysique de Paris, 98bis Bd Arago, 75014, Paris, France

² Faculty of Engineering, Gifu University, 1-1 Yanagido, Gifu 501-1193, Japan

³ Department of Astrophysics, Nagoya University, Furocho, Chikusaku, Nagoya 464-8602, Japan

⁴ LAM, OAMP, Pôle de l'Etoile Site Château-Gombert, 38 rue Frédéric Joliot-Curie, 13388 Marseille Cedex 13, France

⁵ INAF/Osservatorio Astronomico di Trieste, via Tiepolo 11, 34143 Trieste, Italy

Accepted . Received ; Draft printed: August 21, 2018

ABSTRACT

Context. The Ophiuchus cluster, at a redshift $z=0.0296$, is known from X-rays to be one of the most massive nearby clusters, but due to its very low Galactic latitude its optical properties have not been investigated in detail.

Aims. We discuss the optical properties of the galaxies in the Ophiuchus cluster, in particular with the aim of understanding better its dynamical properties.

Methods. We have obtained deep optical imaging in several bands with various telescopes, and applied a sophisticated method to model and subtract the contributions of stars in order to measure galaxy magnitudes as accurately as possible. The colour-magnitude relations obtained show that there are hardly any blue galaxies in Ophiuchus (at least brighter than $r' \leq 19.5$), and this is confirmed by the fact that we only detect two galaxies in H α . We also obtained a number of spectra with ESO-FORS2, that we combined with previously available redshifts. Altogether, we have 152 galaxies with spectroscopic redshifts in the $0.02 \leq z \leq 0.04$ range, and 89 galaxies with both a redshift within the cluster redshift range and a measured r' band magnitude (limited to the Megacam 1×1 deg² field).

Results. A complete dynamical analysis based on the galaxy redshifts available shows that the overall cluster is relaxed and has a mass of $1.1 \cdot 10^{15} M_{\odot}$. The Sernál-Gerbal method detects a main structure and a much smaller substructure that are not separated in projection.

Conclusions. From its dynamical properties derived from optical data, the Ophiuchus cluster seems to be overall a relaxed structure, or at most a minor merger, though in X-rays the central region (radius ~ 150 kpc) may show evidence for merging effects.

Key words. Galaxies: clusters: individual (Ophiuchus), Galaxies: luminosity function

1. Introduction

Though the study of clusters is presently more often devoted to large surveys than to individual objects, it remains useful to analyse clusters individually when they appear to have particularly interesting or uncommon properties. Our attention was drawn on the Ophiuchus cluster, that is the cluster with the second bright-

est X-ray flux, but for which very little is known at optical wavelengths, due to its very low galactic latitude.

Successful attempts have been made by several teams to detect extragalactic objects behind the Milky Way. First, Kraan-Korteweg (1989) searched for individual galaxies in the zone of avoidance at optical wavelengths, and subsequently published a series of papers with more and more detections, including clusters such as the Norma cluster (Kraan-Korteweg et al. 1996, Skelton et al. 2009). Nagayama et al. (2006) performed a near-infrared study of CIZA J1324.7-5736, the second richest cluster of galaxies in the Great Attractor. In X-rays, a systematic search for clusters (and even superclusters) of galaxies was made by Ebeling et al. (2002); in this paper, they give a first catalogue of 73 clusters at redshifts $z < 0.26$ and discuss the identification of the Great Attractor. Other X-ray detections were made by Lopes de Oliveira et al. (2006), who discovered Cl 2334+48 at $z=0.271$ in the Zone of Avoidance in the XMM-Newton archive, and by Mori et al. (2013), who detected the rich cluster Suzaku J1759-3450 at $z=0.13$ behind the Milky Way bulge. The latter cluster was then confirmed by Coldwell et al. (2014), based on infrared data.

At a redshift of 0.0296 (as inferred from our dynamical analysis, see Sect. 4.2), the Ophiuchus cluster was discovered in X-rays by Johnston et al. (1981), who identified the 4U 1708 – 23

[★] Based on observations obtained with MegaPrime/MegaCam (program 10AF02), a joint project of CFHT and CEA/DAPNIA, at the Canada-France-Hawaii Telescope (CFHT) which is operated by the National Research Council (NRC) of Canada, the Institut National des Sciences de l'Univers of the Centre National de la Recherche Scientifique of France, and the University of Hawaii. Based on observations made with ESO Telescopes at the La Silla Paranal Observatory under programme ID 085.A-0016(C). Based on observations obtained at the Southern Astrophysical Research (SOAR) telescope (program 2009B-0340 on SOI/SOAR), which is a joint project of the Ministério da Ciência, Tecnologia, e Inovação (MCTI) da República Federativa do Brasil, the U.S. National Optical Astronomy Observatory (NOAO), the University of North Carolina at Chapel Hill (UNC), and Michigan State University (MSU). This research has made use of the NASA/IPAC Extragalactic Database (NED) which is operated by the Jet Propulsion Laboratory, California Institute of Technology, under contract with the National Aeronautics and Space Administration, and of the SIMBAD database, operated at CDS, Strasbourg, France.

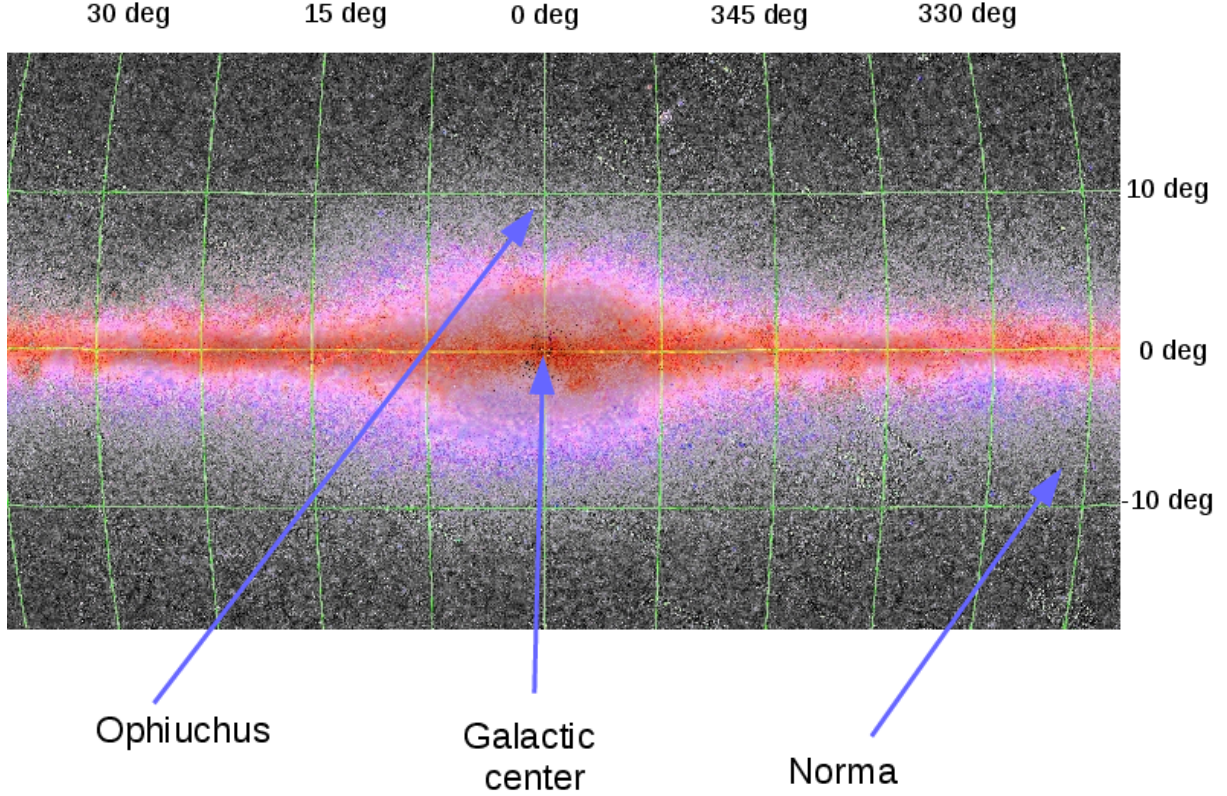


Fig. 1. 2MASS near-infrared image of the Milky Way taken from the Aladin database, showing the positions of the Galactic centre and of the Ophiuchus and Norma clusters.

X-ray source with a cluster of galaxies, and more or less simultaneously at optical wavelengths by Wakamatsu & Malkan (1981) during a search for highly absorbed Galactic globular clusters. It is located in the Zone of Avoidance, not very far from the Great Attractor.

Ophiuchus is mostly known from its X-ray properties, since it is the cluster with the second highest X-ray flux after Perseus (Edge et al. 1990). The first results obtained with ASCA by Matsuzawa et al. (1996) gave for the temperature and metallicity of the X-ray gas the respective values of $kT=9.8$ keV and $Z=0.24 Z_{\odot}$. Based on a mosaic of ASCA data, Watanabe et al. (2001) later derived that Ophiuchus was formed by the merging of two clusters with different iron abundances. They also detected the presence of a small group of galaxies with a colder temperature superimposed on the main cluster. Ophiuchus is part of the sample of clusters detected by Ebeling et al. (2002) in their systematic X-ray search for clusters behind the Milky Way. Ascasibar & Markevitch (2006) showed that the X-ray emission map of Ophiuchus showed the presence of several sharp edges (see their Fig. 1), and argued that these could arise from gas sloshing, set up by a minor merger (as explained in detail by Markevitch & Vikhlinin 2007). The X-ray properties of the central part of Ophiuchus were also analysed in detail by Million et al. (2010), based on Chandra data. These authors showed the existence of a small displacement between the X-ray peak and the cD galaxy (~ 2 kpc), and of several strong features, such as sharp fronts and a very steep temperature gradient between the cool core ($kT=0.7$ keV) and a region located only 30 kpc away

($kT=10$ keV). All these properties suggest that the central regions of Ophiuchus (within 150 kpc of the cluster centre) show evidence for merging, whereas at radii larger than 150 kpc the cluster appears relatively isothermal with a constant metallicity. At even higher energies, Ophiuchus is also part of the sample of nearby clusters where evidence for indirect detection of dark matter has been searched for in Fermi gamma-ray data (Hektor et al. 2013).

Since Ophiuchus is very massive and very old (since it is in the nearby Universe), it can be considered as a perfect example of a cluster where the influence of the cluster on the member galaxies is as strong as can be in the Universe, and it can be taken as a reference for studies of galaxies in clusters such as red sequence or luminosity functions. Ophiuchus is also expected to be one of the clusters with very little star formation, and this motivated our attempt to detect star formation in Ophiuchus by observing it in a narrow band filter containing the $H\alpha$ line at the cluster redshift. However, due to its low Galactic latitude it has not been observed much at optical wavelengths. An analysis was made of the galaxy distribution at very large scale (covering a $12^{\circ} \times 17^{\circ}$ area) by Hasegawa et al. (2000), based on 4021 galaxies with measured spectroscopic redshifts. It was then shown by Wakamatsu et al. (2005) that Ophiuchus has a large velocity dispersion of 1050 ± 50 km s $^{-1}$, agreeing with its high X-ray luminosity, and that several groups or clusters are located within 8° of the cluster, thus forming a structure comparable to a supercluster, close to the Great Attractor. They also found a large

foreground void, implying that it is a continuation of the Local Void.

The difficulty of observing Ophiuchus at optical wavelengths is illustrated in Fig. 1, where we can see that it is even closer to the Galactic centre than the Norma cluster.

For a redshift of 0.0296, Ned Wright’s cosmology calculator¹ gives a luminosity distance of 120.8 Mpc and a spatial scale of 0.585 kpc/arcsec, leading to a distance modulus of 35.54 (assuming a flat Λ CDM cosmology with $H_0 = 71 \text{ km s}^{-1} \text{ Mpc}^{-1}$, $\Omega_M = 0.27$ and $\Omega_\Lambda = 0.73$). The cluster centre is taken to be the position of the cD galaxy: RA=258.1155°, Dec=−23.3698° (J2000.0). This is practically coincident with the peak of the X-ray emission, which is < 3 kpc (0.07 arcmin) away (Million et al. 2010).

The paper is organised as follows. We describe our optical data in Section 2. Results concerning the red sequence detected in colour-magnitude diagrams, star formation, internal structure and dynamical properties are presented in Section 3. The cluster merging state is discussed in Section 4.

2. Optical imaging and spectroscopy

2.1. The data

We obtained optical images in various bands with several telescopes, as summarized in Table 1.

At the Ophiuchus cluster redshift, the $H\alpha$ line falls in the wavelength range covered by the filter adapted to observe the Galactic [SII]6717,6731 emission, so we observed Ophiuchus in this filter with the SOAR telescope and SOI instrument during an observing run dedicated to galaxy clusters in 2009. We also took brief exposures in the Galactic $H\alpha$ and R band filters, to allow a good continuum subtraction in order to derive the $H\alpha$ emission and the star formation rate in the galaxies belonging to the cluster.

2.2. Galaxy selection

As a pilot survey of galaxies, we chose an area of $10.1 \times 9.3 \text{ arcmin}^2$ in RA and DEC centered on the cD galaxy. This area covers the whole VLT and SOAR fields.

At the beginning, we tried an automated galaxy survey, but failed, because too many blended stars were selected erroneously. So instead, we conducted our galaxy survey by eye inspection on the combined g' and r' band images by changing the image brightness and contrast on the ds9 and Gaia viewers. The detections of galaxies of small angular sizes are severely disturbed by many foreground stars. To overcome this difficulty, we made an eye inspection not only of the original images but also of the star-subtracted images (see section 2.3).

On these star-subtracted images, extended objects of small angular sizes show donut-shaped structures around their removed cores, while stars are clearly removed. This is our discrimination between stars and galaxies. For objects difficult to classify, we referred to stellarity indexes deduced from SExtractor and to results of image profiles measured with “imexamine” in IRAF. We selected 225 objects, and later closely re-examined 63 of these objects. Out of those 63 objects, 2/3 are found to be residuals around bright stars (see in section 2.3) or objects with stellarity index > 0.15, and the remaining 1/3 are too faint to obtain reliable stellarity indexes. In Table A.1, we list

162 objects likely to be galaxies with their coordinates and magnitudes. Although the completeness of our survey is difficult to estimate in this complex area, we roughly estimate it to be higher than 70% for galaxies with angular sizes larger than 2.5 to 3 arcsec. Indeed, we independently made a galaxy selection on the VLT image which has the best seeing, and found only two additional galaxies. Some small galaxies lying close to bright stars are missed, because they are buried in diffraction spiders and reflexion residuals of bright stars. Besides, some dwarf galaxies of low surface brightnesses having diameters larger than 3 arcsec are also missed, because they are buried in irregularities of the sky background.

2.3. The method to subtract stars from the images

On our r' band Megacam image, the number density of foreground stars which disturb the galaxy surface photometry in Ophiuchus is found to be about $350 \text{ stars arcmin}^{-2}$, and therefore 100-200 stars are superposed on large bright galaxies. Hence, star-subtraction is essential to achieve good quality galaxy photometry in Ophiuchus.

The present star subtraction procedure is a modified version of the method originally developed by Nagayama et al. (2006). It consists of: 1) extraction of the point spread function (PSF), 2) star subtraction, and 3) cleaning of residuals such as those due to saturated stars or to diffraction on the spider. All these procedures were done using the “DAOPHOT” and “STSDAS” packages in IRAF.

We first describe the extraction of the PSF. Since almost all the stars that should be removed are blended with one another due to the high star density in the Galactic disk, a precise determination of the PSF is crucial. This requires isolated non-blended stars. However, almost all PSF candidate stars within an appropriate magnitude range are blended. So we obtained the final PSF after iterating three times the deblending process for these stars. We detected a spatial variation of the PSF even within a few arcminutes, due not only to the optics of the CFHT wide-field Megacam camera, but also to the different performances of the mosaic CCDs of the camera. Therefore, star subtraction was processed by considering locally extracted PSFs.

Simple star subtraction from an original image is not appropriate, because the profiles of stars superimposed on a galaxy are disturbed by the light of the target galaxy. So, before star subtraction, the galaxy light should be removed from the original image by subtracting a brightness model of the galaxy. This model is extracted from a crude surface photometry of the galaxy with the “ellipse” and “bmodel” tasks in the IRAF STSDAS package. After subtracting this model galaxy from the original image, an image without the galaxy component is created (Fig. 2b). Based on this image, the stellar parameters for star subtraction with the series of PSFs are calculated with the “daofind”, “phot”, etc. tasks. By subtracting these stars to the original sub-image with the “allstar” task, we then obtain a galaxy image without the superposition of foreground stars. Starting with this crudely removed galaxy image, we repeat this loop two or three times (Fig. 2c).

The automated star-subtraction described above is almost perfect for non-saturated stars superposed on galaxies even if they are blended in a complicated way (Fig. 2c). However, this process works very poorly for saturated stars, which are always accompanied by large residuals, e.g., scattered light, spider diffraction patterns, etc. These have irregular shapes, so we are obliged to remove them manually one by one with the “imedit” task in IRAF. If the outer annular zone encircling these resid-

¹ <http://www.astro.ucla.edu/~wright/CosmoCalc.html>

Table 1. Optical imaging observations. The field and pixel size are the values of the reduced dithered and binned images.

Telescope	Instrument	filter	exp. time (s)	field arcmin ²	pixel size arcsec	seeing arcsec
CFHT	Megacam	g'	4830	60×60	0.186	0.9
		r'	2450	60×60	0.186	0.9
VLT	FORS2	z'	90	9.9×9.1	0.252	0.64
SOAR	SOI	R	480	5×5	0.154	1.0
		Gal.H α	360	5×5	0.154	1.0
		Gal.[SII]	2460	5×5	0.154	1.0

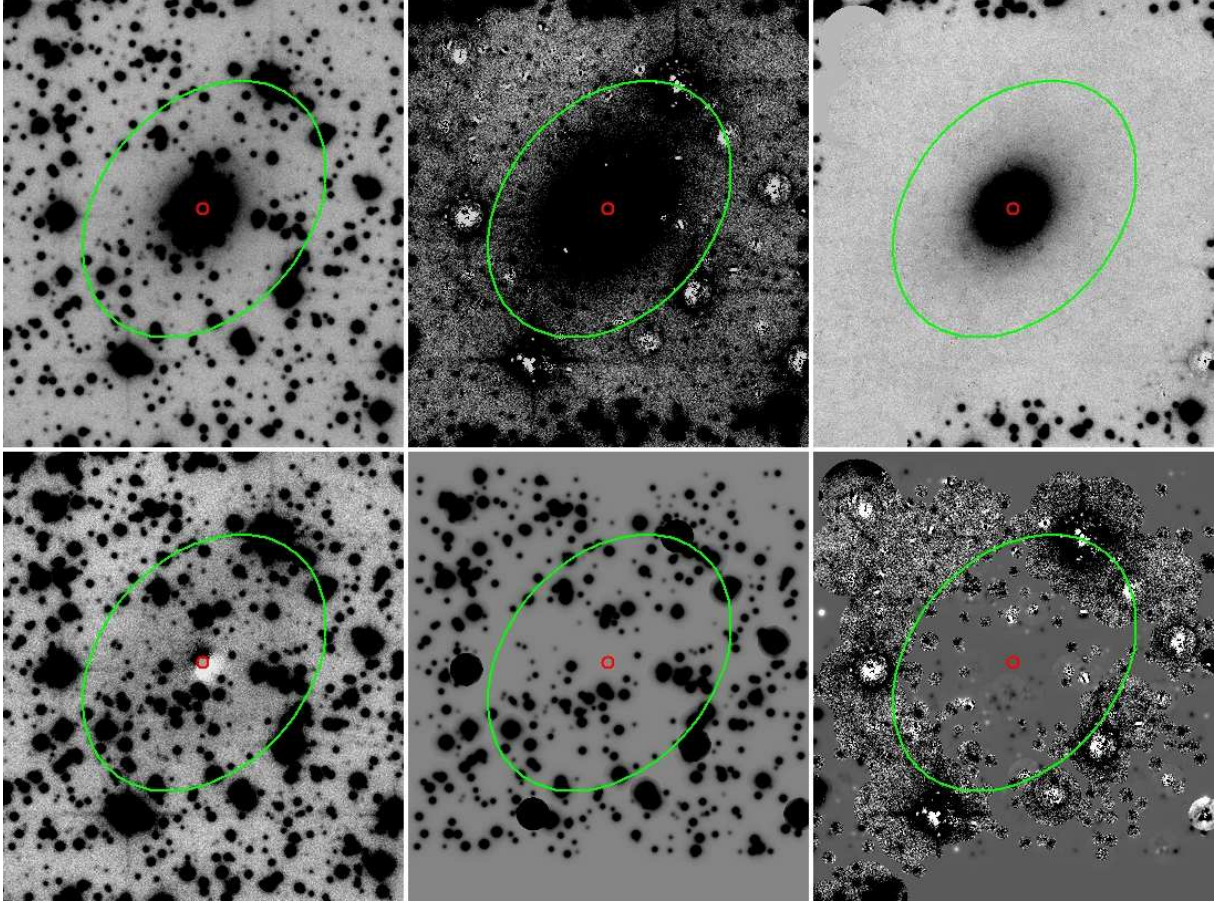


Fig. 2. Images illustrating our method for star-subtraction. The field of view of each image is about 1.1×1.3 arcmin² in the east-west and north-south directions, respectively. The small red circles indicate the position of the nucleus and the green ellipses represent the outer boundary of the galaxy. (a: top left) Original r' band image of 2MASX J17121895-2322192 = OPH 171218.98-232219.1, one of the brightest galaxies. (b: bottom left) Stellar component after subtracting the galaxy model from image (a). This image is almost free of galaxy light, and so appropriate for evaluation of stellar parameters and measuring the PSFs. (c: top middle) Extracted galaxy image after automated star-subtraction with PSFs. Since irregular residuals of saturated stars are not well removed, they disturb the galaxy profile and its surrounding sky area. (d: bottom middle) Image showing the automatically subtracted stars. This is the difference between images (a) and (c) and shows that more than 100 stars superposed on the galaxy are removed. (e: top right) Final image of the galaxy after manual cleaning of residuals around saturated stars in image (c). (f: bottom right) Residuals left after manual cleaning. This is the difference between images (c) and (e).

uals is clean and not disturbed by other residuals, the aperture around the residuals is replaced by an aperture interpolated from this boundary annulus with replacement option “b” in “imedit”. If replacement by interpolation is not appropriate due to neighboring residuals or diffraction patterns, the residual aperture is

substituted, with the replacement option “m”, by a nearby aperture region of similar surface brightness to that of the galaxies (Fig. 2e). This cleaning process is the most delicate and painstaking job, since it must not modify the luminosity profiles and total magnitudes of the galaxies.

The error sources on the star subtraction processes for galaxy photometry are: 1) the subtraction of non-saturated stars with PSFs, 2) the replacement of residuals by interpolation and/or substitution as described above. Besides, bright stars located around the peripheries of galaxies cause uncertainty on the integration boundary for galaxy photometry. For elliptical and S0 galaxies which have smooth and symmetric structures, interpolation and substitution may not be a serious problem, but for spiral galaxies with knotty arms and for interacting galaxies with asymmetric tails and bridges, the situation is more difficult. Fortunately, the Ophiuchus cluster is of cD-type and therefore rich in E and S0 galaxies, and poor in spiral and interacting galaxies. To estimate errors on our photometric measurements, we considered two sets of images with different star-subtractions, and made photometric measurements twice for each band. By comparing these two results, we estimate the errors in the three measured bands as follows:

- 0.07, 0.14, and 0.25 mag for objects with $r' < 19$, $19 < r' < 21$, and $r' > 21$, respectively,
- 0.08, 0.15, and 0.25 mag for objects with $g' < 20$, $20 < g' < 22$, and $g' > 22$ respectively, and
- 0.05, 0.10, and 0.25 mag for objects with $z' < 20$, $20 < z' < 21$, and $z' > 21$ respectively.

These processes are illustrated in Fig. 2.

2.4. The photometric catalogue

After subtracting the star contribution (as described above), we extracted small subimages containing each galaxy and its immediate surroundings, and measured magnitudes and morphological parameters with SExtractor (Bertin & Arnouts 1996). This was done in the g' , r' , and z' bands for all the galaxies located in the field covered by the VLT/FORS2 image. Good quality measurements were achieved for 162 galaxies in the g' , r' , and z' bands respectively. In the region covered by Megacam but not by FORS2, only r' band magnitudes were measured for the galaxies with spectroscopic redshifts, in order to have a sample as large as possible of galaxies with both spectroscopic redshifts and magnitudes, to apply the Serna & Gerbal analysis (see Section 3.3.3). The photometric catalogues are given in Tables A.1 and A.2.

2.5. The spectroscopic catalogue

Redshifts of bright galaxies were obtained covering a very large area on the sky with the AAO 6dF, CTIO 1.5m and Lick 3m telescopes (Wakamatsu et al. 2005), and are listed in Table A.3.

We also obtained spectroscopic data with the ESO VLT/UT1 telescope using FORS2 in two adjacent fields covering the very central region of the cluster, for a total exposure time of 1500s. Spectra were obtained for 55 objects, out of which 54 gave reliable redshifts. Out of these, 17 proved to be galaxy spectra (about 14 belonging to the Ophiuchus cluster) and 37 were stars.

We retrieved redshifts in the NED data base in a region shown in Fig. 3.

We also retrieved a spectrum of the cD galaxy taken by John Huchra at CTIO and measured its velocity to be $cz=8844 \pm 60$ km/s. This is within the error of the systemic velocity of the cluster 8878 ± 76 km/s (as inferred from the dynamical analysis, see Sect. 4.2).

We built a spectroscopic redshift catalogue by combining the Wakamatsu et al. (2005) measurements and our FORS2 measurements, and adding redshifts available in NED for galaxies

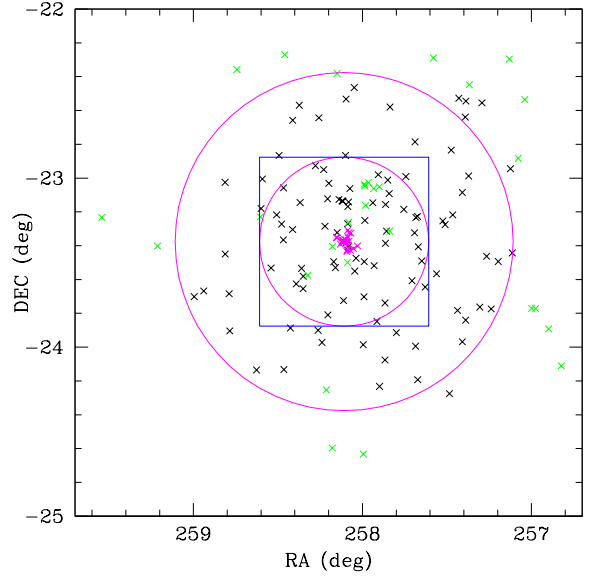


Fig. 3. Spatial distribution of the galaxies with spectroscopic redshifts, color-coded as follows: magenta crosses: our FORS2 measurements, green crosses: Hasegawa measurements, black crosses: values found in NED. The two magenta circles have radii of 0.5 deg (1 Mpc) and 1 deg (2 Mpc) and the blue square shows the size of the Megacam g' and r' band images.

which were not in the two previous catalogues. The resulting catalogue was limited to the redshift range $0.02 \leq z \leq 0.04$, somewhat broader than the cluster range in order not to “lose” galaxies. For the galaxies with several redshift measurements, we took in decreasing priority the FORS2 value, the Wakamatsu et al. (2005) value, and the NED value. Our final redshift catalogue is given in Table A.3 and includes 152 galaxies after eliminating objects with multiple measurements. We estimate the uncertainties on the corresponding cz velocities to be smaller than 280 km s^{-1} for the FORS2 data (see Adami et al. 2011) and between 100 and 300 km s^{-1} for the Wakamatsu et al. (2005) data. The spatial distribution of the galaxies with measured redshifts is displayed in Fig. 3, and the redshift histogram is shown in Fig. 4.

For the galaxies with spectroscopic redshifts located within the CFHT/Megacam field of view but outside the FORS2 field, we performed the star subtraction and measured the magnitudes in the r' band as described above. This gave a catalogue of 89 galaxies with both redshifts and r' band magnitudes within the $1 \times 1 \text{ deg}^2$ Megacam area, to which we applied the Serna & Gerbal software to search for substructures (see section 3.3.3).

3. Results

3.1. The red sequence

For the galaxies with measured g' , r' and z' magnitudes, we drew the three possible colour-magnitude diagrams. These are shown in Fig. 5. We can see from the positions of the galaxies with spectroscopic redshifts in these diagrams that the red sequence is very well defined in all three plots. This confirms the validity of our photometric treatment and star subtraction.

The best fit to the $(g' - r')$ versus r' relation computed with the galaxies brighter than $r' = 20$ is :

$$(g' - r') = (-0.03955 \pm 0.0114)r' + (1.72 \pm 0.21).$$

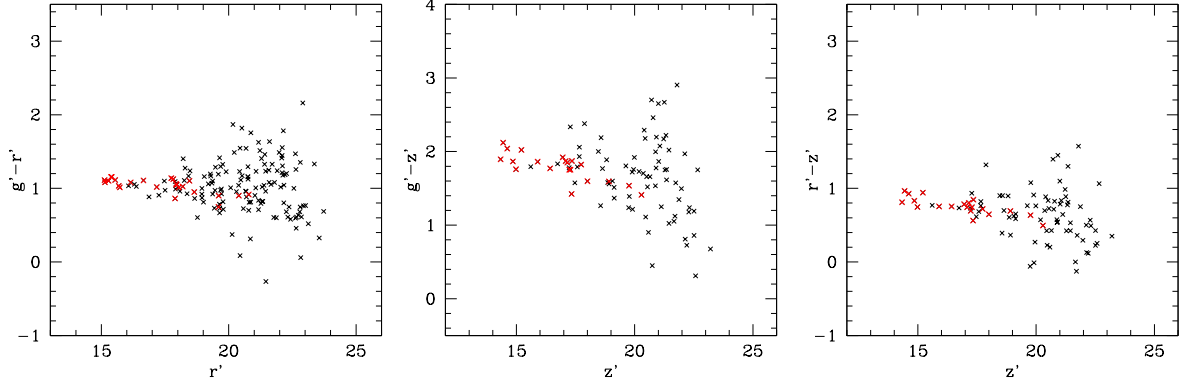


Fig. 5. Colour-magnitude diagrams. The red crosses are the galaxies with spectroscopic redshifts in the $0.02 \leq z \leq 0.04$ range.

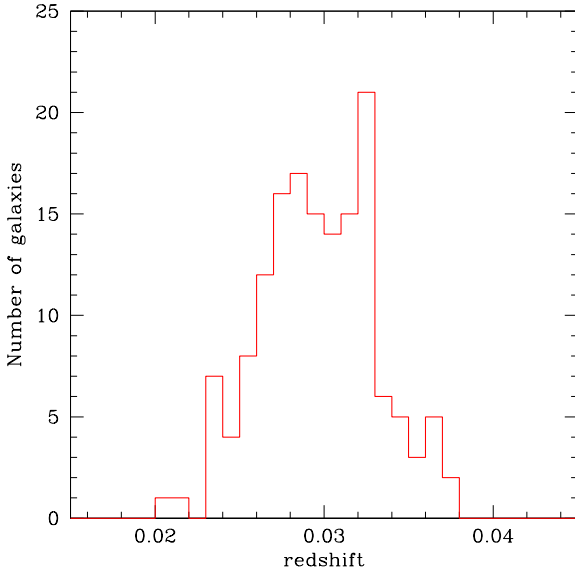


Fig. 4. Spectroscopic redshift histogram for the 152 galaxies of Table A3, with measured redshifts in the $0.02 \leq z \leq 0.04$ redshift range.

This relation can be compared to that estimated for a cluster of comparable richness and redshift, such as Coma. Eisenhardt et al. (2007) give the following relation for Coma (see their Table 13):

$$(B - R) = (-0.055 \pm 0.006)R + (2.259 \pm 0.074).$$

If we translate our relation to B and R magnitudes using the Fukugita et al. (1995) transformations, we find for Ophiuchus:

$$(B - R) = (-0.03955 \pm 0.0114)R + (2.54 \pm 0.21).$$

Though the slope for Ophiuchus is flatter than for Coma, the slopes are consistent within error bars, and the normalisation parameters are of the same order of magnitude.

We can also note from the colour-magnitude relations that there are very few bright blue galaxies in Ophiuchus: in the $(g' - r')$ versus r' diagram, for example, there is not a single galaxy below the red sequence for $r' \leq 19.5$. This result is comparable to that found, for example, in the Coma cluster, where few galaxies bluer than the red sequence are detected (see Fig. 17 in Adami et al. 2007).

This agrees with our idea that Ophiuchus is an “old” cluster, and this is also confirmed by the very small number of galaxies showing ongoing star formation (see next subsection).

3.2. Star formation in Ophiuchus galaxies

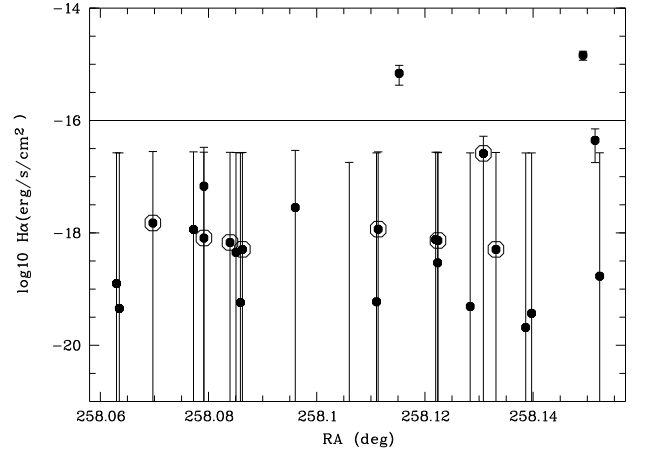


Fig. 6. $H\alpha$ calibrated fluxes (in units of $\text{erg s}^{-1} \text{cm}^{-2}$, in logarithmic scale) versus RA coordinates for all the galaxies detected along the Ophiuchus line of sight. Large open circles are the galaxies observed spectroscopically. The horizontal line shows the detection limit at $10^{-16} \text{ erg s}^{-1} \text{cm}^{-2}$.

As explained in the introduction, we expect the galaxies of Ophiuchus to be in majority old, and therefore lacking star formation. To test this hypothesis, we observed the cluster in a narrow band filter containing $H\alpha$ and [NII] at the cluster redshift, as explained in Section 2. We consider in the following $H\alpha$ and [NII] as a single line noted $H\alpha$.

We first renormalize the $H\alpha$, [SII], and R band SOAR fluxes to take into account the different passbands of these filters and the different exposure times.

For a given object in Ophiuchus, we note I the flux measured in the $H\alpha$ filter. It includes the Milky Way $H\alpha$ flux (MWH α) plus the continuum of the observed object at the filter wavelength (C1). We note II the flux received by the [SII] filter. It includes the Milky Way [SII] flux (MWSII), plus the $H\alpha$ emis-

sion of the observed object ($\text{OH}\alpha$), plus the continuum of the observed object at the filter wavelength (C2).

$$I = C1 + \text{MWH}\alpha \quad (1)$$

$$II = C2 + \text{OH}\alpha + \text{MWSII} \quad (2)$$

Our goal is to measure the $\text{H}\alpha$ emission of the observed object: $\text{OH}\alpha$.

From Fig. 8 of Haffner et al. (1999), we estimate the ratio between the Milky Way $\text{H}\alpha$ and $[\text{SII}]$ emissions to be 4.7 ± 0.3 at the Ophiuchus position:

$$\text{MWH}\alpha / \text{MWSII} = 4.7 \pm 0.3 \quad (3)$$

Moreover, we can safely assume that $C1 \approx C2$, since the wavelengths of the $\text{H}\alpha$ and $[\text{SII}]$ filters are very similar:

$$C1 = C2 = C \quad (4)$$

Combining equations (1) to (4), we have:

$$\text{OH}\alpha = II - (I/4.7) - C * (1. - (1./4.7)) \quad (5)$$

We must now estimate C (our $\text{H}\alpha$ and $[\text{SII}]$ images and our spectra are not flux calibrated). We assume this value to be the same for all the Ophiuchus galaxies, a reasonable hypothesis since we are considering a very homogeneous population of cluster galaxies. We then select the galaxies for which no $\text{H}\alpha$ line is visible in our spectra. In this case, equation (5) becomes:

$$C = (II - (I/4.7)) / (1. - (1./4.7)) \quad (6)$$

We then estimate C for the previously selected Ophiuchus galaxies with no $\text{H}\alpha$ emission, and apply this value to all the considered objects. We therefore have a direct access to the uncalibrated $\text{OH}\alpha$ flux with equation (5) for all the observed objects.

To have a calibrated flux, we compare our SOAR R-band and CFHTLS r' fluxes and apply the corresponding zero point to $\text{OH}\alpha$ fluxes. We then generate Fig. 6. Considering the galaxies for which we have a spectrum (we did not detect any $\text{H}\alpha$ lines in our spectroscopic sample), we estimate the maximum value below which the $\text{H}\alpha$ emission is not detectable to be about $10^{-16} \text{ erg s}^{-1} \text{ cm}^{-2}$.

Only two galaxies in Fig. 6 show a significant $\text{H}\alpha$ emission. Their coordinates are $(258.149^\circ, -23.3223^\circ)$ and $(258.115^\circ, -23.3696^\circ)$ and their respective $\text{H}\alpha$ fluxes are 1.446×10^{-15} and $0.692 \times 10^{-15} \text{ erg s}^{-1} \text{ cm}^{-2}$.

After converting $\text{H}\alpha$ fluxes into star formation rates (hereafter SFR) with the Kennicutt (1998) relation, our detection limit translates to $1.5 \times 10^{-3} \text{ M}_\odot \text{ yr}^{-1}$, a fairly low value. Even the two galaxies in which we do detect $\text{H}\alpha$ have fairly low SFRs of the order of $0.02 \text{ M}_\odot \text{ yr}^{-1}$ and $0.01 \text{ M}_\odot \text{ yr}^{-1}$ respectively.

We therefore conclude that the Ophiuchus galaxies have very low SFRs, as expected.

3.3. The cluster internal structure and dynamics

3.3.1. Selection of spectroscopic cluster members

We examined the positions of the galaxies in the “blue” peak (i.e. those with $0.02 \leq z < 0.032$) and those in the “red” peak ($0.032 \leq z \leq 0.04$) of Fig. 4, but were not able to separate them spatially. Therefore, if the blue and red distributions correspond to two clusters in the process of merging, the merger must be

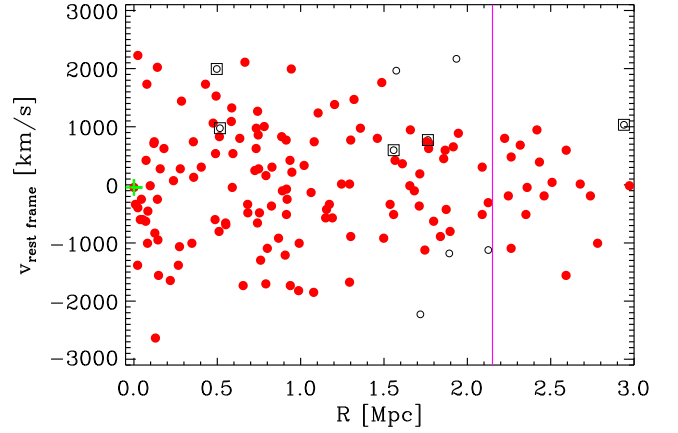


Fig. 7. Rest-frame velocities vs. distances from the cluster center for all galaxies with redshifts in the cluster region. Filled (red) dots identify cluster members; the green-crossed red dot is the cD galaxy. The empty circles identify the 5 interlopers found by the shifting gapper procedure. The empty circles within squares identify the 5 interlopers found by the adaptive-kernel procedure. Note that some of them are nearly coincident in projected phase-space, hence the symbols are superposed.

taking place along a direction close to perpendicular to the plane of the sky.

To identify the cluster members among the 152 galaxies with measured redshift, we use the ‘shifting gapper’ method of Fadda et al. (1996). This method searches for gaps of 1000 km s^{-1} in the velocity distributions, within overlapping radial intervals of $0.4 \text{ h}^{-1} \text{ Mpc}$ (corresponding to 0.56 Mpc for our adopted cosmology). These gaps are used to separate interlopers from cluster members. Five galaxies are identified as interlopers by this procedure.

We then refine our membership identification by another procedure which is similar to the one developed by Biviano et al. (1996) for the Coma cluster. We determine two adaptive kernel maps of the galaxy number densities, one unweighted, and another weighted by the galaxy rest-frame velocities. The ratio of the two maps defines an adaptive kernel map of local velocities. We then run 1000 bootstrap resamplings to establish the significance of the adaptive kernel map of galaxy velocities, at each galaxy position, $\sigma_{boot,i}$ (see Appendix A of Biviano et al. 1996 for more details). When the adaptive kernel value of the velocity at the i -th galaxy position deviates from zero at more than $3\sigma_{boot,i}$, we reject galaxy i from the list of cluster members. We reject five galaxies by this procedure, so we are left with a total of 142 cluster members.

The projected-phase space distribution of all galaxies with spectroscopic redshifts in the cluster region is shown in Fig. 7. It displays a decrease of velocity dispersion with increasing distance from the cluster center, as seen in many nearby clusters (e.g. Biviano et al. 1997).

3.3.2. Dynamical analysis

The histogram of rest-frame velocities for the cluster members is shown in Fig. 8. The mean redshift and velocity dispersion of the cluster members are $\bar{z} = 0.0296 \pm 0.0003$ and $\sigma_v = 954^{+58}_{-55} \text{ km s}^{-1}$, respectively (derived using the robust biweight esti-

mator, see Beers et al. 1990). Our new estimate of σ_v is significantly lower than the value obtained by Wakamatsu et al. ($1050 \pm 50 \text{ km s}^{-1}$). Using our new values of \bar{z} and σ_v , we draw the corresponding Gaussian distribution in Fig. 8. A Kolmogorov-Smirnov test (e.g. Press et al. 1992) gives a probability of 0.82 that the observed velocity distribution is a random draw of the Gaussian distribution. In other terms, the observed distribution is statistically indistinguishable from a Gaussian. This is generally taken as evidence for a relaxed dynamical configuration (e.g. Girardi et al. 1993; Ribeiro et al. 2011).

Additional support for a dynamically relaxed status of the cluster also comes from the position of the cD in projected phase-space (Beers et al. 1991). It is in fact spatially coincident with the peak of the X-ray emission, and its velocity is consistent within the errors with the mean cluster velocity, $\Delta v = 47 \pm 97 \text{ km s}^{-1}$.

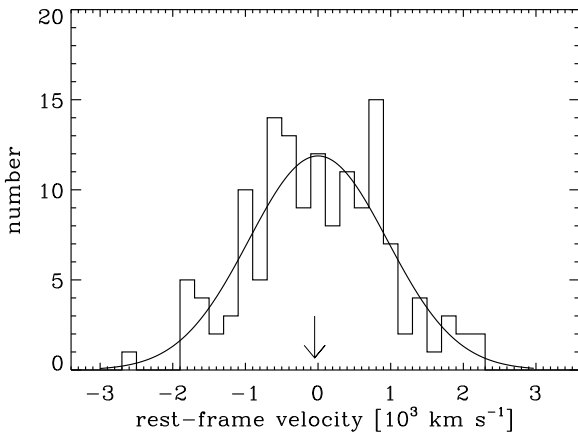


Fig. 8. Histogram of the rest-frame velocities of the identified cluster members. The best-fitting gaussian is overplotted. The arrow indicates the velocity of the cD galaxy.

It is possible to obtain a first, preliminary estimate of the cluster mass from the σ_v estimate, via the scaling relation of Munari et al. (2013; eq. 1): $M_{200} = 9.3 [8.1, 10.7] \times 10^{14} M_{\odot}$, corresponding to $r_{200} = 2.0 [1.89, 2.07] \text{ Mpc}$, where the values in brackets correspond to the 1σ confidence intervals².

We proceed by estimating the cluster mass profile using the MAMPOSSt technique of Mamon et al. (2013). This technique performs a Maximum Likelihood fit of selected mass and velocity-anisotropy models, to the projected phase-space distribution of cluster members.

We consider three models for the mass distribution: 1) Burkert (1995; 'Bur'), 2) Hernquist (1990; 'Her'), and 3) the popular Navarro et al. (1996; 'NFW'). The three models are characterized by different logarithmic slopes of their mass density profiles, 0, -1, and -1 near the center, and -3, -4, -3 at large radii, for Bur, Her, and NFW, respectively. Each of these models is characterized by two free parameters, the virial radius r_{200} , and the scale radius. The NFW scale radius corresponds to the radius where the logarithmic slope of the mass density pro-

² The virial radius r_{200} is the radius of a sphere with mass overdensity 200 times the critical density of the Universe at the cluster redshift. The virial mass M_{200} is directly related to r_{200} via $M_{200} \equiv 100 H_z^2 r_{200}^3 / G$, where H_z is the Hubble constant at the cluster mean redshift.

Table 2. Results of the MAMPOSSt analysis

$r_{200} [\text{Mpc}]$	2.1 [1.8, 2.2]
$r_{-2} [\text{Mpc}]$	0.7 [0.5, 1.4]
β_{∞}	0.8 [0.4, 1.0]
$M_{200} [10^{14} M_{\odot}]$	11.1 (6.8, 13.7)

Notes. Results are shown for the best-fit models Her+T. Values in brackets are 1σ lower and upper confidence levels.

file equals -2, and we therefore denote it by r_{-2} . The Bur scale radius approximately corresponds to $2/3 r_{-2}$, while the Her scale radius corresponds exactly to $2 r_{-2}$. For the sake of homogeneity, we rescale the scale radii of the Bur and Her model to always quote the results for r_{-2} .

We consider two models for the velocity anisotropy profile,

$$\beta(r) = 1 - \frac{\sigma_{\theta}^2(r) + \sigma_{\phi}^2(r)}{2\sigma_r^2(r)} = 1 - \frac{\sigma_{\theta}^2(r)}{\sigma_r^2(r)} \quad (7)$$

where $\sigma_{\theta}, \sigma_{\phi}$ are the two tangential components, and σ_r the radial component, of the velocity dispersion, and the last equivalence is obtained in the case of spherical symmetry. Negative, null, and positive values of β correspond to galaxy orbits that are tangential, isotropic, and radial, respectively. One of the two models ('C') assumes constant $\beta(r)$ at all radii. The other ('T' from Tiet et al. 2007) is of the form: $\beta(r) = \beta_{\infty} r / (r + r_{-2})$. The two models are both characterized by only one free parameter, the constant value of β for the C model, and β_{∞} for the T model, since r_{-2} in this model is the same scale radius parameter of the mass models.

In MAMPOSSt, and in general in all dynamical analyses based on the Jeans equation (Binney & Tremaine 1987), knowledge of the radial dependence of the completeness of the spectroscopic sample is required. An unknown or uncorrected-for radial-dependent incompleteness would bias the determination of the number density profile of the tracer of the gravitational potential, which enters the Jeans equation. On the other hand, the velocity distribution of the tracers is in general unaffected by incompleteness problems, since observations do not generally select cluster members in velocity space. In the case of Ophiuchus, an estimate of the radial completeness of the spectroscopic sample is not available, because of the stellar crowded field. As a consequence we must make the assumption that the number density profile of the tracers and the mass density profile of the cluster have the same shape, and are therefore characterized by the same scale parameter, r_{-2} . This case was already considered by Mamon et al. (2013), and denoted 'TLM' (for 'Tied Light and Mass'). They showed that MAMPOSSt can work very well also within this restrictive assumption.

We find that Her+T provides the best-fit among the six combinations of the three mass and the two anisotropy models. However, all models are statistically acceptable. The best-fit values for the three free parameters $r_{200}, r_{-2}, \beta_{\infty}$ are listed in Table 2, with their uncertainties, obtained by marginalizing each parameter with respect to the other two. For completeness we also translate the constraints on r_{200} into constraints on the cluster mass, M_{200} . The values of β_{∞} indicate that the galaxy orbits are mostly radially elongated in this cluster.

In Fig. 9 we show the constraints obtained by MAMPOSSt in the r_{-2} vs. r_{200} plane. The uncertainties on the r_{200} value of the best-fit models, Her+T, are larger than the differences among the

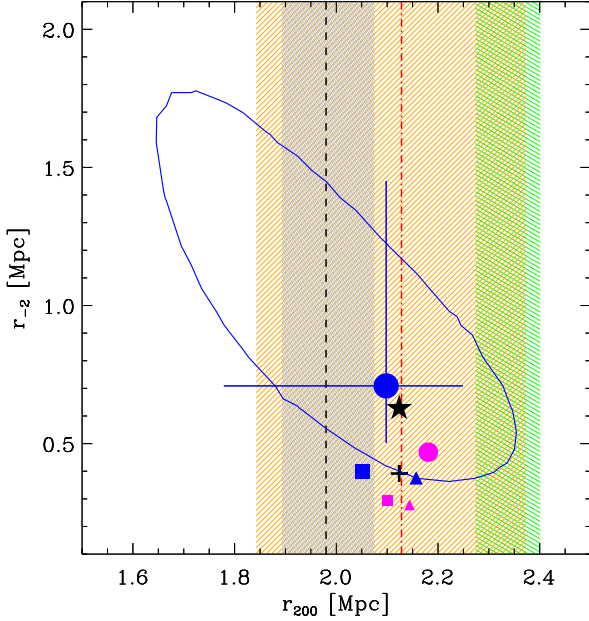


Fig. 9. Results of the dynamical analysis in the r_{-2} vs. r_{200} plane. The squares, dots, and triangles indicate the best-fit values obtained by MAMPOSSt for the Her, NFW, and Bur mass models. Magenta and blue symbols are for the C and T $\beta(r)$ models, respectively. The symbol size is proportional to the MAMPOSSt likelihood. The ellipse indicates the 1σ uncertainty on the best-fit MAMPOSSt results, after marginalization over the velocity anisotropy parameter. The error bars are obtained upon marginalization of each parameter over the other two. The cross indicates the mean of the values obtained by the different models considered for the MAMPOSSt analysis. The vertical black dashed line indicates the value of r_{200} obtained from the cluster velocity dispersion using the scaling relation of Munari et al. (2013). The shaded grey region indicates the uncertainties on this value. The vertical red dash-dotted line indicates the value of r_{200} obtained with the Caustic technique of Diaferio & Geller (1997). The shaded orange region indicates the uncertainties on this value. The shaded green region indicates the range of r_{200} as obtained from the range of X-ray temperatures found in the literature (see text), using the scaling relation of Vikhlinin et al. (2009). The star symbol represents the theoretical expectation from De Boni et al. (2013), obtained adopting the average value of r_{200} .

values obtained with the different models. On the other hand, some of the r_{-2} values are more than 2σ below the value obtained with the Her+T model. The average $[r_{200}, r_{-2}]$ value (the '+' symbol in the figure) among the different models is in fact below the value of the best-fit model. However, it is remarkable that the latter is in excellent agreement with the theoretically predicted value obtained using the concentration-mass relation of De Boni et al. (2013, the star symbol in the figure), and the average value of r_{200} , because the theoretical estimate comes from a concentration-mass relation. Given r_{200} , one has the mass, and from the mass, the concentration. Given the concentration and r_{200} , one has r_{-2} .

We also display in Fig. 9 the r_{200} values obtained from σ_v using the scaling relation of Munari et al. (2013). The relatively narrow confidence region (gray shaded area in the figure) only

reflects the uncertainty in the theoretical value of the scaling relation. In reality, this is an underestimate, because several systematic uncertainties are not taken into account (see Munari et al. 2013 for more details). Considering that the formal uncertainties on the σ_v -determined r_{200} values are smaller than the real ones, these values can be considered to be in fair agreement with the MAMPOSSt results.

The MAMPOSSt results are also in agreement with the r_{200} values obtained by applying the Caustic technique of Diaferio & Geller (1997; see also Diaferio 1999) to our spectroscopic dataset (red line and orange shaded region in Fig. 9). This technique does not require the assumption of dynamical equilibrium, but suffers from an uncertain calibration which is generally determined using numerical simulations. We adopt here the caustic mass calibration factor of Gifford et al. (2013), $\mathcal{F}_\beta = 0.65$.

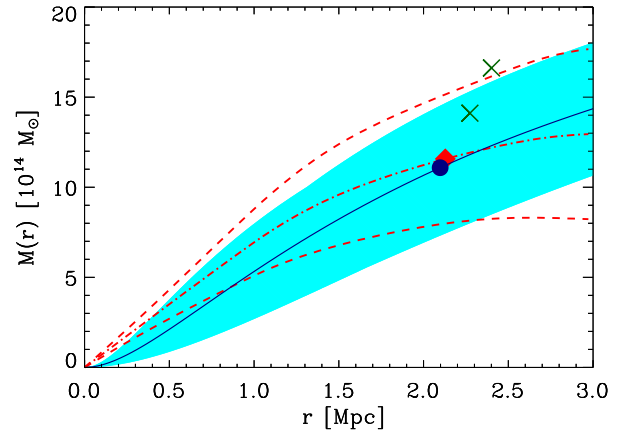


Fig. 10. The cluster mass profile as obtained from MAMPOSSt (solid blue line) within its 1σ confidence interval (dashed cyan region). The blue dot is the location of $[r_{200}, M_{200}]$. The dash-dotted and dashed red lines indicate the cluster mass profile obtained from the Caustic technique and, its 1σ upper and lower limits respectively. The red diamond is the location of $[r_{200}, M_{200}]$. The green 'X' symbols indicate the locations of $[r_{200}, M_{200}]$ obtained using the observed range of cluster T_X and the scaling relation of Vikhlinin et al. (2009).

Fig. 10 shows the two mass profiles obtained by MAMPOSSt and the Caustic technique. They are in agreement within their uncertainties, except in the central region, where the Caustic mass profile exceeds the MAMPOSSt-derived one. This is due to a well known bias of the Caustic technique, that tends to overestimate the mass profile in the central regions (Serra et al. 2011).

Overall we conclude that there is a very good agreement in the mass and mass profile estimates obtained with different techniques based on the projected phase-space galaxy distribution in the cluster.

It is also possible to determine r_{200} (and therefore also M_{200}) from the cluster X-ray temperature. For this we use the scaling relation of Vikhlinin et al. (2009) with fixed exponent $\alpha = 1.5$, and the most recent and accurate determinations of the cluster X-ray temperatures, $T_X = 9.1$ keV (Nevalainen et al. 2009) and $T_X = 9.7$ keV (Fujita et al. 2008). The derived range of values accounts for the uncertainties in the normalization of the scaling relation of Vikhlinin et al. (2009). As it can be seen from

Figs. 9 and 10 the allowed range of r_{200} (and M_{200}) values obtained from the X-ray temperatures, overlaps with the range of values we infer from the kinematic analysis. The X-ray derived values tend however to be somewhat higher than the values derived from the kinematic analysis. Possibly, the observed cluster T_X is somewhat increased by a past collision between a cluster and a subcluster.

3.3.3. The presence of substructures

We made a dynamical analysis with the Serna-Gerbal technique (hereafter SG, 1996 release, Serna & Gerbal 1996), a hierarchical code (based on spectroscopic redshifts and optical magnitudes) designed to detect substructures in the optical. The SG method has proved to be quite powerful to show evidence for substructures in nearby clusters (see Abell 496: Durret et al. 2000; Coma: Adami et al. 2005; Abell 85: Boué et al. 2008) as well as in more distant ones (Guennou et al. 2014). We applied it here to the catalogue of 89 galaxies with both redshifts and r' band magnitudes within the $1 \times 1 \text{ deg}^2$ Megacam area.

Assuming a value of the mass to luminosity ratio (here taken to be 100), the SG method allows to estimate the masses of the structures that it detects. Although the absolute masses are not accurate (the typical uncertainty is clearly larger than $10^{14} M_\odot$), the mass ratios of the various structures are well determined (Guennou et al. 2014). The SG method has also been extensively tested on simulations by Guennou (2012), in particular concerning the effect of undersampling on mass determinations.

One of the parameters that can be chosen is the minimum number n of galaxies in a structure. We have applied the SG method with $n=10$ and $n=5$ and find similar results in both cases. The total mass of the system is found to be $M_{\text{tot}} = 3.7 \times 10^{14} M_\odot$. This estimate refers to the mass within the Megacam area, i.e. within a radius of $\approx 1 \text{ Mpc}$. We will divide the masses of the detected substructures by this quantity to estimate the percentages of this total mass included in each of the substructures.

We find one large structure S1 of 75 galaxies and a much smaller structure S2 of 13 galaxies. The mass ratios of these two structures to the main cluster component are 0.67 and 0.065. Structure S1 can itself be divided into two substructures, S11 and S12, with 65 and 10 galaxies respectively, and S11 can itself be divided into two structures. In all cases we find a large substructure and a much smaller one, implying that only minor mergers can be occurring. These results are illustrated in Fig. 11, where an adaptive kernel map of the main structure is drawn, with the galaxies of the two structures S1 and S2 superimposed.

As an illustration of the relative significance of the structures detected by the SG method, we refer the reader to Fig. 5 of Guennou et al. (2014), showing the percentage of substructures detected by the SG method as a function of the spectroscopic sampling.

The SG dynamical analysis therefore clearly confirms that Ophiuchus is not a fully relaxed cluster, but any merger must have been minor, so it has not strongly affected the dynamics of the cluster.

4. Discussion and conclusions

We now discuss the merging status of Ophiuchus. As mentioned above, only Watanabe et al. (2001) claim that it is a major merger, based on a temperature map drawn from ASCA data. On the other hand, several studies, including the one presented here, strongly suggest that Ophiuchus is only the result of a minor merger.

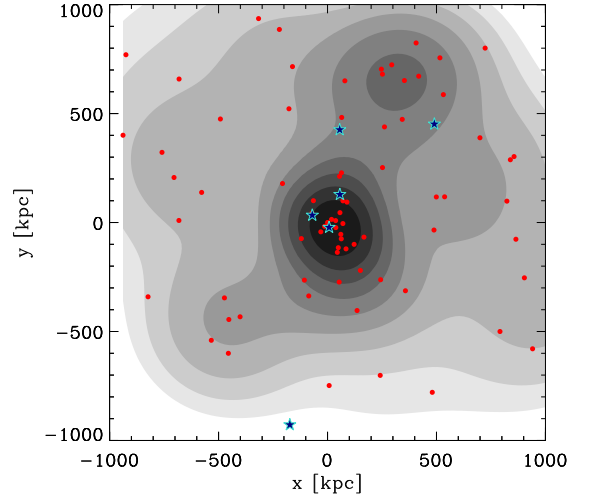


Fig. 11. Adaptive-kernel number density map of the galaxies in structure 1 of the SG substructure analysis. The contours are logarithmically spaced. Red dots indicate the positions of the galaxies belonging to this group. Blue stars indicate the positions of the galaxies belonging to group 2 in the SG substructure analysis.

From our data, there are several converging indices showing that Ophiuchus is not a cluster strongly perturbed by merging events. First, the center of the cD galaxy coincides with the X-ray peak. Second, the velocity distribution is Gaussian, another evidence for global relaxation, and third the cluster mass derived from the Jeans equation agrees with the cluster mass computed with the caustic method, still another evidence for relaxation. The masses derived from X-rays are a little higher, but still consistent. Finally, the SG analysis does not imply strong subclustering, given that a large fraction of the mass is not associated to any substructure.

Ophiuchus was originally believed to be a merging cluster, based on an X-ray temperature map derived from ASCA data (Watanabe et al. 2001) and showing two very hot regions to the West and South of the center, some 20 arcmin away. The comparison of this map with simulations suggested that a merger had occurred about 1 Gyr ago. However, based on Suzaku data, these results were contradicted by Fujita et al. (2008), who did not detect the huge temperature variations found by Watanabe et al. (2001). On the contrary, they found that Ophiuchus was a cool core cluster, with isothermal gas (with a temperature $kT = 9.7^{+0.9}_{-1.0} \text{ keV}$) beyond 50 kpc from the cluster centre. We can note however that even if Ophiuchus is a cool core cluster, it may have experienced a minor merger, as indicated for example by the simulations of Burns et al. (2008). Fujita et al. (2008) also wrote that the iron-line ratios measured on the X-ray spectra indicated that the ICM had reached an ionization equilibrium state, implying that the cluster could not be a major merger. However, this time based on Chandra data, Million et al. (2010) found evidence for a collision from the comet-like morphology of the X-ray emission near the cluster centre. They interpreted the very strong temperature gradient, from 0.7 keV within 1 kpc to 10 keV at 30 kpc, as due to the fact that the outer part of the cool core has been stripped by ram pressure.

Other results are consistent with Ophiuchus being a minor merger. For example, Murgia et al. (2009) have detected a mini radio-halo around the cluster dominant radio galaxy, with a radio emissivity typical of haloes in merging clusters. However, according to Zandanel et al. (2014), the mini-halo in Ophiuchus has a radio luminosity much lower than giant radio halos in merging clusters, so this suggests that any merger can only have been a minor one. The hard X-ray component detected with XMM-Newton by Nevalainen et al. (2009) is indicative of relativistic electrons, which are also responsible for the mini radio halo. The hypothesis of a minor merger agrees with the fact that Hamer et al. (2012) measured an offset between optical line emission and the BCG (about 2 kpc), and suggested it could be due to the merger-induced motion of the ICM relative to the BCG. From their data, the merger must have occurred recently, about 20–100 Myr ago.

Adding this evidence together, it seems likely that a merger has indeed occurred (probably quite recently), but that it was not a major merger, and perhaps since Ophiuchus is so massive, this merger has not perturbed much its dynamical state, though it may have affected the intra-cluster medium to some extent. At smaller scale than the entire cluster, some perturbations have been observed, such as an object located 1.7 kpc from the BCG showing low ionization optical emission lines and interpreted by Edwards et al. (2009) as a large cloud falling towards the BCG. This system would then be comparable to that described in the optical IFU observations of NGC 4696 by Farage et al. (2010). However, they cannot perturb the cluster properties, as for example confirmed by the lack of star forming galaxies.

Acknowledgements. We thank A. Boselli for discussions and the referee for suggestions. FD acknowledges long-term support from CNES.

References

- Adami C., Biviano A., Durret F., Mazure A. 2005, *A&A* 443, 17
 Adami C., Durret F., Mazure A. et al. 2007, *A&A* 462, 411
 Adami C., Mazure A., Pierre M. et al. 2011, *A&A* 526, 18
 Ascasibar Y. & Markevitch M. 2006, *ApJ* 650, 102
 Beers T.C., Flynn K. & Gebhardt K. 1990, *AJ* 100, 32
 Beers T.C., Gebhardt K., Forman W., Huchra J.P., Jones C. 1991, *AJ* 102, 1581
 Bertin E., Arnouts S. 1996, *A&AS* 117, 393
 Binney J. & Tremaine S. 1987, “Galactic dynamics”, Princeton University Press, p. 747
 Biviano A., Durret F., Gerbal D. et al. 1996, *A&A* 311, 95
 Biviano A., Katgert P., Mazure A. et al. 1997, *A&A* 321, 84
 Boué G., Durret F., Adami C., Mamon G., Ilbert O., Cayatte V., 2008b, *A&A* 489, 11
 Burkert A. 1995, *ApJ* 447, L25
 Burns J.O., Hallman E.J., Gantner B., Motl P.M., Norman M.L. 2008, *ApJ* 675, 1125
 Coldwell G., Alonso S., Duplancic F. et al. 2014, *A&A* 569, 49
 De Boni C., Ettori S., Dolag K., Moscardini L. 2013, *MNRAS* 428, 2921
 Diaferio A. & Geller M.J. 1997, *ApJ* 481, 633
 Diaferio A. 1999, *MNRAS* 309, 610
 Durret F., Adami C., Gerbal D., Pislari V. 2000, *A&A* 356, 815
 Ebeling H., Mullis C.R., Tully R.B. 2002, *ApJ* 580, 774
 Edge A.C., Stewart G.C., Fabian A.C., Arnaud K.A. 1990, *MNRAS* 245, 559
 Edwards L.O.V., Robert C., Mollá M., McGee S.L. 2009, *MNRAS* 396, 1953
 Eisenhardt P.R., De Propriis R., Gonzalez A.H. et al. 2007, *ApJS* 169, 225
 Fadda D., Girardi M., Giuricin G., Madirossian F., Mezzetti M. 1996, *ApJ* 473, 670
 Farage C.L., McGregor P.J., Dopita M.A., Bicknell G.V. 2010, *ApJ* 724, 267
 Fujita Y., Hayashida K., Nagai M. et al. 2008, *PASJ* 60, 1133
 Fukugita M., Shimasaku K., Ichikawa R. 1995, *PASJ* 107, 945
 Gifford D., Miller C., & Kern N. 2013, *ApJ* 773, 116
 Girardi M., Biviano A., Giuricin G., Madirossian F., Mezzetti M. 1993, *ApJ* 404, 38
 Guennou L. 2012, PhD Thesis, Université de Marseille-Provence, France
 Guennou L., Adami C., Durret F. et al. 2014, *A&A* 561, 112
 Haffner L.M., Reynolds R.J., Tufte S.L. 1999, *ApJ* 523, 223
 Hamer S.L., Edge A.C., Swinbank A.M. et al. 2012, *MNRAS* 421, 3409
 Hasegawa T., Wakamatsu K., Malkan M. et al. 2000, *MNRAS* 316, 326
 Hektor A., Raidal M., Tempel E. 2013, *ApJ* 762, 22
 Hernquist L. 1990, *ApJ* 356, 359
 Johnston M.D., Bradt H.V., Doxsey R.E. et al. 1981, *ApJ* 245, 799
 Kennicutt, Jr. R. C. 1998, *ARA&A*, 36, 189
 Kraan-Korteweg R.C. 1989, *Reviews in Modern Astronomy* v.2, 119
 Kraan-Korteweg R.C., Woudt P.A., Cayatte V. et al. 1996, *Nature* 379, 519
 Lopes de Oliveira R., Lima Neto G.B., Mendes de Oliveira C., Janot-Pacheco E., Motch C. 2006, *A&A* 459, 415
 Mamon G.A., Biviano A. & Boué G. 2013, *MNRAS* 429, 3079
 Markevitch M. & Vikhlinin A. 2007, *Physics Reports* 443, 1
 Matsuzawa H., Matsuoka M., Ikebe Y., Mihara T. 1996, *PASJ* 48, 565
 Million E.T., Allen S.W., Werner N., Taylor G.B. 2010, *MNRAS* 405, 1624
 Mori H., Maeda Y., Furuzawa A., Haba Y., Ueda Y. 2013, *PASJ* 65, 102
 Munari E., Biviano A., Borgani S., Murante G., Fabjan D. 2013, *MNRAS* 430, 2638
 Murgia M., Govoni F., Markevitch M. et al. 2009, *A&A* 499, 679
 Nagayama T., Woudt P.A., Wakamatsu K. et al. 2006, *MNRAS*, 368, 534
 Navarro J.F., Frenk C.S., & White S.D.M. 1996, *ApJ* 462, 563
 Nevalainen J., Eckert D., Kaastra J., Bonamente M., Kettula K. 2009, *A&A* 508, 1161
 Press W. H., Teukolsky S.A., Vetterling W.T., Flannery B.P. 1992, “Numerical Recipes in C”, Cambridge University Press, 2nd edition
 Ribeiro A.L.B., Lopes P.A.A. & Trevisan M. 2011, *MNRAS* 413, L81
 Serna A. & Gerbal D. 1996, *A&A* 309, 65
 Serra A.L., Diaferio A., Murante G., Borgani S. 2011, *MNRAS* 412, 800
 Skelton R.E., Woudt P.A., Kraan-Korteweg R.C. 2009, *MNRAS* 396, 2367
 Tifft O., Combes F., Angus G.W., Famaey B., Zhao H.S. 2007, *A&A* 476, L1
 Vikhlinin A., Burenin R.A., Ebeling H. et al. 2009, *ApJ* 692, 1033
 Wakamatsu K. & Malkan M.A. 1981, *PASJ* 33, 57
 Wakamatsu K., Malkan M.A., Nishida M.T. et al. 2005, in “Nearby Large-Scale Structures and the Zone of Avoidance”, ASP Conference Series 329, 189
 Watanabe M., Yamashita K., Furuzawa A., Kunieda H., Tawara Y. 2001, *PASJ* 53, 605
 Zandanel F., Frommer C., Prada F. 2014, *MNRAS* 438, 124

Appendix A: Catalogues

The photometric catalogue in the g' , r' and z' bands of the galaxies located within the VLT/FORS2 field is given in Table A.1 for 162 objects.

The photometric catalogue in the r' band of the galaxies with a measured spectroscopic redshift but outside the VLT/FORS2 field is given in Table A.2 for 65 galaxies.

The full catalogue of 152 spectroscopic redshifts (covering a region larger than our images) is given in Table A.3.

Table A.1. Photometric catalogue in the r' , g' and z' bands in the central region covered by the FORS2 z' band image. The columns are: (1) running number (the galaxies indicated with * have a spectroscopic redshift given in Table A.3), (2) object OPH name, (3) and (4) RA and DEC (J2000.0), (5), (6) and (7) r' , g' and z' band magnitudes (the symbols : and :: respectively indicate a relatively large and a large uncertainty), (8) quality of the galaxy classification (1: almost definitely a galaxy, 2: probably a galaxy, 3: possibly a galaxy; when the object is certainly a galaxy, there is no indication in this column), (9) notes, other identifications and comments (poor photometric condition around object, e.g., bright stars or diffraction on the spider, are expressed as 1, 2, and 3).

Running number	OPH name	RA (J2000.0)	DEC (J2000.0)	r'	g'	z'	Quality	Note
1	OPH J171205.08-232033	258.02116	-23.34253	16.872:	17.756:			1
2	OPH J171205.41-232050	258.02255	-23.34746	20.756	22.050			
3	OPH J171205.68-232158	258.02367	-23.36624	21.588	22.669		1	
4	OPH J171205.85-232149	258.02439	-23.36387	17.261:	18.167:			1
5	OPH J171206.10-231818	258.02541	-23.30512	20.681	22.224			
6	OPH J171206.16-232218	258.02567	-23.37174	20.869	22.623	20.445		
7	OPH J171206.17-232251	258.02570	-23.38082	19.684:	20.981:	19.744:		3
8*	OPH J171207.00-232405	258.02918	-23.40148	16.152	17.233	15.211		2MASX J17120697-2324053
9	OPH J171207.25-232501	258.03020	-23.41707	20.220	21.707	19.951		
10	OPH J171207.33-232532	258.03055	-23.42559	19.898	21.124	19.909		
11	OPH J171207.41-231826	258.03088	-23.30737	21.409	22.736		1	
12	OPH J171207.45-232030	258.03106	-23.34188	16.375	17.400	15.606		
13	OPH J171207.62-231809	258.03174	-23.30255	23.017	23.783		3	
14	OPH J171208.13-231835	258.03386	-23.30983	20.526	21.697			1
15	OPH J171208.31-232255	258.03461	-23.38196	20.786:	21.487:	20.585:	3	3
16	OPH J171208.39-232606	258.03497	-23.43500	18.951	19.823	18.559:		star near nucleus
17	OPH J171208.50-231908	258.03543	-23.31901	18.087	19.047	17.472		
18	OPH J171208.68-232236	258.03615	-23.37671	22.142	23.924::	21.255	1	
19	OPH J171208.74-232219	258.03641	-23.37204	19.718	20.644	19.131	3	
20	OPH J171208.94-231801	258.03725	-23.30048	22.662	23.271		3	
21	OPH J171209.04-231808	258.03767	-23.30242	20.475	21.588			
22	OPH J171209.78-232020	258.04073	-23.33899	22.828	22.887:	22.576	2	
23	OPH J171209.98-231845	258.04158	-23.31256	20.665	21.627			
24	OPH J171210.04-231753	258.04184	-23.29820	18.946	19.868			
25	OPH J171210.12-232445	258.04218	-23.41262	21.576	22.824	21.703:	1	
26	OPH J171210.37-231756	258.04320	-23.29896	18.773:	19.377:			2
27	OPH J171210.90-231754	258.04541	-23.29859	20.444::	20.530::		1	2
28	OPH J171211.08-232251	258.04615	-23.38083	22.161	22.964	21.349	2	
29	OPH J171211.12-232504	258.04635	-23.41799	21.450	22.410	20.876	2	
30	OPH J171211.13-232604	258.04636	-23.43456	22.321	22.930	22.203:	3	
31	OPH J171211.15-232415	258.04647	-23.40442	19.712	20.703	18.815	1	1
32	OPH J171211.18-232500	258.04657	-23.41668	20.694	21.577	20.467		
33	OPH J171211.23-232006	258.04679	-23.33513	21.661	22.713	21.661:	3	
34	OPH J171211.50-231821	258.04793	-23.30600	20.681	21.640			
35	OPH J171211.52-232557	258.04802	-23.43265	18.422	19.590	17.658		
36	OPH J171212.06-232434	258.05026	-23.40950	21.075	22.306	20.648	3	1
37	OPH J171212.33-231824	258.05139	-23.30683	21.170	22.007		1	
38	OPH J171212.35-231743	258.05147	-23.29536	17.913	18.902			
39	OPH J171212.43-232158	258.05179	-23.36620	22.110	23.415	20.714	3	
40	OPH J171212.51-232119	258.05213	-23.35536	23.728	24.415	22.664	3	
41*	OPH J171212.61-232501	258.05253	-23.41716	20.396	21.297	19.761		
42	OPH J171212.76-232546	258.05317	-23.42969	21.266	22.060	20.540	2	
43	OPH J171214.15-231911	258.05897	-23.31989	22.734	23.369	22.509		
44	OPH J171215.13-232322	258.06306	-23.38954	19.280	20.475	18.915		
45	OPH J171215.24-232159	258.06352	-23.36655	20.758	21.915	20.186		
46	OPH J171215.60-231833	258.06501	-23.30928	18.949	19.948			
47	OPH J171216.10-231806	258.06707	-23.30168	22.428	23.008		3	
48*	OPH J171216.71-231931	258.06963	-23.32539	17.178	18.196	16.424		
49	OPH J171216.92-231946	258.07048	-23.32957	21.802	22.882	21.017		
50*	OPH J171217.22-232537	258.07174	-23.42704	17.895	18.757	17.333		
51	OPH J171217.56-232550	258.07316	-23.43066	20.851:	21.164	19.774		1
52	OPH J171217.95-232440	258.07479	-23.41120	22.095	23.309	21.734	1	
53	OPH J171218.18-232455	258.07574	-23.41533	22.101	23.655	21.003::	3	
54	OPH J171218.50-232042	258.07709	-23.34512	17.474	18.573	16.740		
55	OPH J171218.51-231914	258.07714	-23.32057	22.212	23.398	21.227	1	
56	OPH J171218.71-231836	258.07794	-23.31010	21.227	22.740		1	
57	OPH J171218.82-232525	258.07840	-23.42361	21.418	22.879	20.883	2	
58*	OPH J171218.97-231921	258.07904	-23.32266	17.932	18.992	17.238		
59*	OPH J171218.98-232219	258.07910	-23.37198	15.541	16.654	14.614		2MASX J17121895-2322192
60	OPH J171219.27-232046	258.08030	-23.34625	21.602	23.237	20.777	3	

Table A.1. Continued.

Running number	OPH name	RA (J2000.0)	DEC (J2000.0)	r'	g'	z'	Quality	Note
61	OPH J171219.30-232012	258.08041	-23.33684	22.368	23.115	20.919:	2	
62	OPH J171219.32-232059	258.08051	-23.34981	22.621	23.217	21.870	1	
63*	OPH J171219.91-232418	258.08294	-23.40510	15.405	16.560	14.440		2MASX J17121989-2324187
64	OPH J171220.07-232001	258.08362	-23.33384	21.770	22.375	21.125	3	
65*	OPH J171220.15-232343	258.08397	-23.39538	18.032	19.042	17.288		
66	OPH J171220.37-232551	258.08487	-23.43096	21.449	22.682	20.905		
67	OPH J171220.41-232124	258.08504	-23.35678	18.259	19.366	17.575		2
68*	OPH J171220.68-232054	258.08615	-23.34832	18.458	19.561	17.738		
69*	OPH J171220.70-231831	258.08626	-23.30878	15.386	16.540			2MASX J17122070-2318318
70	OPH J171221.47-231745	258.08947	-23.29602	21.317	22.336		1	semi-stellar
71	OPH J171221.47-231954	258.08947	-23.33189	21.287	22.693	20.402		
72	OPH J171221.55-232305	258.08979	-23.38498	22.808	23.554	22.316	3	
73*	OPH J171221.60-232528	258.08999	-23.42448	18.650	19.600	18.003		
74*	OPH J171222.14-232604	258.09225	-23.43459	15.143	16.225	14.331		2MASX J17122214-2326048
75*	OPH J171223.04-232252	258.09598	-23.38113	16.654	17.762	15.900		2MASX J17122302-2322518
76*	OPH J171223.09-232156	258.09622	-23.36565	20.783	21.699	20.288		
77	OPH J171223.10-232112	258.09623	-23.35345	19.684	20.660	19.060		1
78	OPH J171223.42-232053	258.09760	-23.34826	22.270	23.472	21.976	1	
79	OPH J171223.68-231813	258.09867	-23.30384	18.663	19.526			
80	OPH J171223.70-232313	258.09875	-23.38697	21.340	22.164	20.505	3	
81	OPH J171224.18-231828	258.10075	-23.30798	17.898	18.991			
82	OPH J171224.73-231821	258.10304	-23.30586	19.642	20.308			
83*	OPH J171225.43-232146	258.10595	-23.36299	17.743	18.881	16.959		
84	OPH J171226.61-232511	258.11089	-23.41990	22.098	23.544	21.323	3	
85	OPH J171226.62-232425	258.11093	-23.40713	21.460::	21.194::	20.744::	3	2
86	OPH J171226.79-232236	258.11164	-23.37674	19.481	20.768	18.580		
87*	OPH J171226.83-232249	258.11181	-23.38038	17.826	18.952	17.082		
88*	OPH J171226.86-234327	258.11194	-23.72424	16.621::				
89	OPH J171227.25-232453	258.11354	-23.41477	19.787	20.502	19.135		
90	OPH J171227.36-232515	258.11402	-23.42091	22.263:	22.945:	22.135:	2	
91*	OPH J171227.36-232225	258.11402	-23.37373	19.602::	20.350::			superposed on cD galaxy
92*	OPH J171227.72-232211	258.11549	-23.36978	15.284:	16.386:	13.484		2MASX J17122774-2322108 cD
93	OPH J171228.62-231930	258.11924	-23.32521	22.648	23.106	21.349		
94	OPH J171228.66-231959	258.11942	-23.33316	21.902	23.142	21.067	2	
95	OPH J171229.14-232419	258.12141	-23.40546	19.465	20.438	18.859		
96	OPH J171229.39-231920	258.12246	-23.32233	19.199	20.259	17.880:		1
97*	OPH J171229.40-232241	258.12249	-23.37805	18.194	19.219	17.348		
98	OPH J171229.48-232123	258.12285	-23.35654	18.212	19.614	17.279		
99	OPH J171229.94-232632	258.12476	-23.44238	19.368	20.290			
100	OPH J171230.29-232604	258.12619	-23.43444	19.340	20.410	18.641		
101	OPH J171230.44-232057	258.12682	-23.34921	21.873	22.473	21.449	3	
102	OPH J171230.92-231850	258.12885	-23.31406	22.081	23.493		3	
103	OPH J171230.96-232320	258.12899	-23.38910	20.748	21.906	19.986		
104	OPH J171231.02-232448	258.12927	-23.41346	23.554:	23.880:	23.204:	3	
105	OPH J171231.13-232211	258.12971	-23.36971	20.390	21.431	19.626	1	semi-stellar
106*	OPH J171231.55-232324	258.13146	-23.38999	17.959	19.006	17.156		
107	OPH J171231.81-231742	258.13254	-23.29525	22.789	23.471			
108	OPH J171231.97-232043	258.13319	-23.34550	18.483	19.721	17.662		
109	OPH J171232.03-232529	258.13345	-23.42494	22.936	23.699	22.509	3	
110	OPH J171233.25-231841	258.13854	-23.31157	19.647	20.375			
111	OPH J171233.36-232203	258.13898	-23.36771	21.705	23.032	21.282		
112	OPH J171233.54-232120	258.13973	-23.35579	19.366	20.466	18.465	1	semi-stellar
113	OPH J171234.01-232159	258.14170	-23.36643	23.363::	24.694::	21.790::	3	
114	OPH J171235.46-231726	258.14777	-23.29077	21.386	22.427			
115	OPH J171235.64-232449	258.14852	-23.41374	20.806	21.617	19.896		
116	OPH J171235.74-232624	258.14892	-23.43999	19.592	20.784			
117*	OPH J171235.80-231920	258.14916	-23.32229	15.684	16.718	14.852		2MASX J17123580-2319208
118	OPH J171235.86-232409	258.14943	-23.40257	21.983	23.471	21.451	1	
119	OPH J171235.91-231954	258.14964	-23.33191	22.855	23.466	22.287	3	
120	OPH J171236.01-232335	258.15006	-23.39318	21.061	22.067	20.363		

Table A.1. Continued.

Running number	OPH name	RA (J2000.0)	DEC (J2000.0)	r'	g'	z'	Quality	Note
121	OPH J171236.21-232255	258.15089	-23.38199	22.620	24.090	22.120	3	
122	OPH J171236.31-232632	258.15128	-23.44226	20.866	21.679			
123*	OPH J171236.39-232114	258.15163	-23.35395	15.727	16.740	14.981		2MASX J17123638-2321138
124*	OPH J171236.61-232056	258.15254	-23.34913	19.605	20.505	18.912		
125	OPH J171237.09-232412	258.15454	-23.40351	17.959	19.011	17.230:		at field edge in z-band
126	OPH J171237.32-231737	258.15548	-23.29364	19.779	20.597			2
127	OPH J171237.37-231753	258.15572	-23.29807	22.910	25.070:		1	
128	OPH J171237.55-232520	258.15647	-23.42226	21.172	21.882			
129	OPH J171237.64-232623	258.15683	-23.43980	15.671::				2
130	OPH J171237.65-232333	258.15686	-23.39253	22.128	23.306		3	
131	OPH J171237.95-232230	258.15811	-23.37511	18.365	19.292			
132	OPH J171238.19-232029	258.15914	-23.34154	19.642	21.057			
133	OPH J171238.41-232133	258.16004	-23.35923	22.639	23.895		3	
134	OPH J171238.81-232220	258.16171	-23.37238	19.764	21.090			
135	OPH J171239.26-232430	258.16358	-23.40850	19.010	19.822			
136	OPH J171239.38-232224	258.16410	-23.37359	20.166	22.034			
137	OPH J171239.42-232240	258.16423	-23.37790	21.170	22.796			
138	OPH J171239.83-232005	258.16597	-23.33486	19.438	20.168			
139	OPH J171240.15-232505	258.16730	-23.41831	16.299	17.354			
140	OPH J171241.01-232639	258.17087	-23.44419	15.6::				3
141	OPH J171241.03-232537	258.17097	-23.42717	18.288	19.563			
142	OPH J171241.44-232335	258.17265	-23.39326	19.296	20.464			
143	OPH J171241.56-231950	258.17315	-23.33065	20.428	21.657		1	semi-stellar
144	OPH J171241.73-232501	258.17387	-23.41709	20.760	21.885			
145	OPH J171242.25-232003	258.17605	-23.33418	16.067	17.101			
146	OPH J171242.31-232338	258.17629	-23.39414	22.810	24.163		1	
147*	OPH J171242.60-232417	258.17751	-23.40484	15.127	16.239			2MASX J17124256-2324167
148	OPH J171242.83-231938	258.17846	-23.32733	20.134:	20.507:			1
149	OPH J171243.02-232452	258.17926	-23.41457	22.558	23.558		3	
150	OPH J171243.33-232558	258.18054	-23.43303	19.637	20.421			
151	OPH J171243.61-232125	258.18170	-23.35716	20.077	21.085			
152	OPH J171243.64-232038	258.18185	-23.34398	22.171	23.214		3	
153	OPH J171243.78-232541	258.18242	-23.42828	20.517:	22.335:		3	
154	OPH J171244.00-232056	258.18334	-23.34908	22.043	23.059			
155	OPH J171244.23-232124	258.18428	-23.35667	19.042	20.202			
156	OPH J171244.24-232300	258.18434	-23.38354	20.446	21.992			
157	OPH J171245.51-231900	258.18961	-23.31673	21.310	22.130		1	
158	OPH J171245.61-232019	258.19004	-23.33875	17.504	18.478			
159	OPH J171246.11-231819	258.19212	-23.30538	21.027	21.930		3	
160	OPH J171246.33-231738	258.19306	-23.29391	20.302	21.258			
161	OPH J171247.16-231854	258.19650	-23.31515	20.575	21.300			
162	OPH J171247.68-232127	258.19865	-23.35757	23.125	23.644		3	

Table A.2. Objects with a measured spectroscopic redshift but outside the VLT/FORS2 area. The columns are: (1) running number, (2) object name, (3) and (4) RA and Dec (J2000.0), (5) r' band magnitude, (6) other identification.

Running number	OPH name	RA (J2000.0)	DEC (J2000.0)	r'	other name
1	OPH J171014.78-233404	257.56158	-23.56784	15.672	2MASX J17101464-2333587
2	OPH J171030.94-233839	257.62893	-23.64431	15.886	2MASX J17103094-2338399
3	OPH J171035.72-232925	257.64883	-23.49036	16.611	2MASX J17103573-2329248
4	OPH J171040.67-232422	257.66945	-23.40633	16.179	2MASX J17104066-2324228
5	OPH J171041.87-231335	257.67446	-23.22643	16.308	2MASX J17104188-2313348
6	OPH J171044.00-231400	257.68333	-23.23336	16.284	2MASX J17104398-2313598
7	OPH J171045.89-231923	257.69121	-23.32331	16.067	2MASX J17104588-2319238
8	OPH J171049.53-233624	257.70638	-23.60683	15.982	2MASX J17104954-2336246
9	OPH J171058.45-225927	257.74355	-22.99086	15.660	2MASX J17105842-2259266
10	OPH J171101.25-231107	257.75522	-23.18542	16.108	
11	OPH J171121.22-231849	257.83843	-23.31380	14.801	2MASX J17112119-2318497
12	OPH J171122.02-230529	257.84176	-23.09154	16.834	2MASX J17112206-2305297
13	OPH J171124.03-230042	257.85012	-23.01172	15.968	2MASX J17112403-2300427
14	OPH J171125.89-231851	257.85789	-23.31420	16.174	2MASX J17112592-2318507
15	OPH J171127.15-230922	257.86313	-23.15616	16.399	6dF J1711272-230922
16	OPH J171127.20-232309	257.86332	-23.38601	16.263	2MASX J17112722-2323097
17	OPH J171128.02-234420	257.86677	-23.73902	16.333	2MASX J17112802-2344197
18	OPH J171136.00-230306	257.89998	-23.05172	15.595	2MASX J17113598-2303057
19	OPH J171137.53-225846	257.90636	-22.97946	15.445	2MASX J17113750-2258457
20	OPH J171143.43-233106	257.93097	-23.51835	15.718	2MASX J17114344-2331057
21	OPH J171144.13-230339	257.93386	-23.06101	15.082	2MASX J17114409-2303397
22	OPH J171145.31-230844	257.93881	-23.14556	15.574	2MASX J17114534-2308447
23	OPH J171151.29-230136	257.96372	-23.02688	15.080	2MASX J17115130-2301363
24	OPH J171155.39-230942	257.98079	-23.16187	15.242	2MASX J17115542-2309423
25	OPH J171156.54-231501	257.98557	-23.25032	15.682	2MASX J17115651-2315013
26	OPH J171156.63-230250	257.98594	-23.04726	16.319	2MASX J17115666-2302503
27	OPH J171157.23-230211	257.98846	-23.03648	15.201	2MASX J17115724-2302113
28	OPH J171157.46-232938	257.98941	-23.49403	16.537	2MASXi J1711574-232938
29	OPH J171157.70-234207	257.99041	-23.70216	16.380	2MASX J17115766-2342073
30	OPH J171209.06-232826	258.03774	-23.47404	16.078	2MASX J17120908-2328263
31	OPH J171210.92-233300	258.04550	-23.55018	16.513	2MASX J17121090-2333003
32	OPH J171217.94-230342	258.07475	-23.06182	16.875	2MASX J17121796-2303422
33	OPH J171219.71-230828	258.08212	-23.14121	16.239	2MASX J17121970-2308288
34	OPH J171219.79-231541	258.08247	-23.26150	15.288	2MASX J17121976-2315418
35	OPH J171220.86-231004	258.08691	-23.16801	15.332	2MASX J17122085-2310048
36	OPH J171220.94-231610	258.08727	-23.26970	16.492	2MASX J17122092-2316108
37	OPH J171221.13-232957	258.08805	-23.49916	15.290	2MASX J17122113-2329568
38	OPH J171223.90-225159	258.09960	-22.86646	16.598	2MASXi J1712239 -225159
39	OPH J171227.78-230811	258.11574	-23.13658	16.431	2MASX J17122782-2308108
40	OPH J171228.80-230803	258.11998	-23.13422	16.183	2MASX J17122884-2308038
41	OPH J171233.29-230734	258.13870	-23.12631	15.720	2MASX J17123325-2307348
42	OPH J171238.46-233145	258.16023	-23.52930	15.784	2MASX J17123843-2331458
43	OPH J171240.94-232942	258.17060	-23.49512	16.140	2MASX J17124097-2329427
44	OPH J171247.65-230151	258.19854	-23.03087	16.905	2MASX J17124767-2301517
45	OPH J171249.23-234834	258.20511	-23.80948	17.600	
46	OPH J171249.58-230720	258.20657	-23.12233	15.373	2MASX J17124957-2307207
47	OPH J171253.26-231705	258.22191	-23.28487	16.724	
48	OPH J171255.07-225700	258.22945	-22.95003	15.507	2MASX J17125506-2257000
49	OPH J171306.82-225535	258.27843	-22.92641	15.904	2MASX J17130678-2255350
50	OPH J171317.53-233429	258.32303	-23.57474	15.152	2MASX J17131749-2334290
51	OPH J171323.91-233450	258.34963	-23.58056	16.369	2MASX J17132392-2334506
52	OPH J171324.19-233914	258.35081	-23.65413	16.105	2MASX J17132420-2339146
53	OPH J171326.45-233201	258.36020	-23.53382	16.095	2MASX J17132646-2332016
54	OPH J171328.44-230840	258.36852	-23.14461	16.167	2MASX J17132844-2308406
55	OPH J171334.02-233733	258.39177	-23.62591	16.105	2MASX J17133402-2337336
56	OPH J171339.33-231814	258.41387	-23.30412	15.599	
57	OPH J171351.94-230328	258.46642	-23.05802	16.522	2MASX J17135195-2303286
58	OPH J171352.23-232155	258.46763	-23.36535	15.925	2MASX J17135221-2321556
59	OPH J171354.89-231618	258.47871	-23.27181	16.110	2MASX J17135490-2316186
60	OPH J171358.48-225156	258.49365	-22.86564	15.859	2MASX J17135847-2251566
61	OPH J171401.72-231302	258.50717	-23.21740	15.035	2MASX J17140172-2313026
62	OPH J171409.76-233153	258.54066	-23.53157	15.028	2MASX J17140971-2331536
63	OPH J171422.04-230018	258.59185	-23.00507	16.762	2MASX J17142206-2300182
64	OPH J171423.86-231048	258.59942	-23.18012	15.653	2MASX J17142386-2310482
65	OPH J171424.83-231347	258.60345	-23.22983	14.735	2MASX J17142479-2313472

Table A.3. Spectroscopic redshift catalogue. The columns are: (1) running number (for objects with *, photometric data are given in Tables A1 (VLT/FORS2 area) and A2 (outside the VLT/FORS2 area), (2) object name, (3) spectroscopic redshift, (4) reference to the origin of the redshift: 1 for our FORS2 data, 2 for our 6df, CTIO 1.5m, and Lick 3m data (Wakamatsu et al. 2005), and 3 for NED.

Number	name	redshift	reference
1	2MASX J17071767-2406391	0.0332	3
2	2MASX J17073583-2353321	0.0317	3
3	2MASX J17075426-2346173	0.0295	3
4	2MASX J17075972-2346163	0.0320	3
5	2MASX J17080961-2232072	0.0290	3
6	2MASX J17081885-2252587	0.0259	3
7	2MASX J17082726-2326327	0.0327	2
8	2MASX J17082979-2256397	0.0258	2
9	2MASX J17083142-2217447	0.0296	3
10	2MASX J17084712-2329350	0.0275	2
11	2MASX J17085724-2346260	0.0269	2
12	2MASX J17090361-2327449	0.0329	2
13	2MASX J17091029-2233179	0.0279	2
14	2MASX J17091341-2345468	0.0321	2
15	2MASX J17092831-2226505	0.0310	3
16	2MASX J17092925-2259155	0.0296	2
17	2MASX J17093322-2232395	0.0290	2
18	2MASX J17093341-2350245	0.0220	2
19	2MASX J17093394-2238225	0.0307	2
20	2MASX J17093813-2358058	0.0312	2
21	2MASX J17093810-2305055	0.0265	2
22	2MASX J17094318-2231395	0.0324	2
23	1RXS J170944.9-234658	0.0364	2
24	2MASX J17095181-2313038	0.0323	2
25	2MASX J17095391-2250048	0.0293	2
26	2MASX J17095655-2416307	0.0313	2
27	2MASX J17100247-2316308	0.0277	2
28	2MASX J17100581-2315138	0.0285	2
29*	2MASX J17101464-2333587	0.0277	2
30	2MASX J17101930-2217218	0.0298	3
31*	2MASX J17103094-2338399	0.0339	2
32*	2MASX J17103573-2329248	0.0237	2
33*	2MASX J17104066-2324228	0.0265	2
34	2MASX J17104160-2411341	0.0371	2
35*	2MASX J17104188-2313348	0.0255	2
36*	2MASX J17104398-2313598	0.0325	2
37	2MASX J17104452-2359408	0.0279	2
38	2MASX J17104522-2247088	0.0357	2
39*	2MASX J17104588-2319238	0.0307	2
40*	2MASX J17104954-2336246	0.0311	2
41*	2MASX J17105842-2259266	0.0233	2
42*	OPH J171101.25-231107	0.0259	2
43	2MASX J17111189-2354508	0.0266	2
44	2MASX J17112078-2234457	0.0322	2
45*	2MASX J17112119-2318497	0.0274	3
46*	2MASX J17112206-2305297	0.0302	2
47*	2MASX J17112403-2300427	0.0279	2
48*	2MASX J17112592-2318507	0.0325	2
49*	6dF J1711272-230922	0.0369	2
50*	2MASX J17112722-2323097	0.0315	2
51	2MASX J17112794-2404348	0.0311	2
52*	2MASX J17112802-2344197	0.0294	2
53	2MASX J17113574-2413554	0.0317	2
54*	2MASX J17113598-2303057	0.0238	3
55*	2MASX J17113750-2258457	0.0288	2
56	OPH J171139.58-235053	0.0322	2
57*	2MASX J17114344-2331057	0.0333	2
58*	2MASX J17114409-2303397	0.0274	3
59*	2MASX J17114534-2308447	0.0334	2
60*	2MASX J17115130-2301363	0.0331	3

Table A.3. Continued.

Number	name	redshift	reference
61*	2MASX J17115542-2309423	0.0269	3
62*	2MASX J17115651-2315013	0.0322	2
63*	2MASX J17115666-2302503	0.0305	3
64*	2MASX J17115724-2302113	0.0326	3
65*	2MASXi J1711574-232938	0.0301	2
66*	2MASX J17115766-2342073	0.0340	2
67	2MASX J17115865-2438004	0.0297	3
68	2MASX J17115882-2359083	0.0347	2
69*	2MASX J17120697-2324053	0.0318	1
70*	2MASX J17120908-2328263	0.0249	2
71*	2MASX J17121090-2333003	0.0307	2
72	2MASX J17121160-2227513	0.0319	2
73*	OPH J171212.61-232501	0.0306	1
74*	OPH J171216.71-231931	0.0206	1
75*	OPH J171217.22-232537	0.0243	1
76*	2MASX J17121796-2303422	0.0237	2
77*	OPH J171218.97-231921	0.0322	1
78*	2MASX J17121895-2322192	0.0275	1
79*	2MASX J17121970-2308288	0.0276	2
80*	2MASX J17121976-2315418	0.0299	3
81*	2MASX J17121989-2324187	0.0296	2
82*	OPH J171220.15-232343	0.0262	1
83*	OPH J171220.68-232054	0.0311	1
84*	2MASX J17122070-2318318	0.0366	1
85*	2MASX J17122085-2310048	0.0356	2
86*	2MASX J17122092-2316108	0.0240	2
87*	2MASX J17122113-2329568	0.0306	3
88*	OPH J171221.60-232528	0.0268	1
89*	2MASX J17122214-2326048	0.0264	1
90*	2MASX J17122302-2322518	0.0288	2
91*	OPH J171223.09-232156	0.0276	1
92	2MASX J17122328-2231578	0.0318	2
93*	2MASXi J1712239-225159	0.0292	2
94*	OPH J171225.43-232146	0.0283	1
95*	OPH J171226.86-234327	0.0306	2
96*	OPH J171226.83-232249	0.0373	1
97*	OPH J171227.36-232225	0.0285	1
98*	2MASX J17122774-2322108	0.0295	2
99*	2MASX J17122782-2308108	0.0349	2
100*	2MASX J17122884-2308038	0.0365	2
101*	OPH J171229.40-232241	0.0249	1
102*	OPH J171231.55-232324	0.0276	1
103*	2MASX J17123325-2307348	0.0330	2
104*	2MASX J17123580-2319208	0.0321	2
105	2MASX J17123583-2222498	0.0279	3
106*	2MASX J17123638-2321138	0.0356	1
107*	OPH J171236.61-232056	0.0281	1
108*	2MASX J17123843-2331458	0.0262	2
109*	2MASX J17124097-2329427	0.0346	2
110*	2MASX J17124256-2324167	0.0288	3
111	2MASX J17124278-2435477	0.0243	3
112*	OPH J171249.23-234834	0.0365	2
113*	2MASX J17124767-2301517	0.0318	2
114*	2MASX J17124957-2307207	0.0273	2
115	2MASX J17125134-2415096	0.0282	3
116*	OPH J171253.26-231705	0.0260	2
117*	2MASX J17125506-2257000	0.0323	2
118	2MASX J17125738-2358196	0.0239	2
119	OPH J171301.84-223836	0.0317	2
120	2MASX J17130287-2354020	0.0282	2

Table A.3. Continued.

Number	name	redshift	reference
121*	2MASX J17130678-2255350	0.0234	2
122*	2MASX J17131749-2334290	0.0295	3
123*	2MASX J17132392-2334506	0.0324	2
124*	2MASX J17132420-2339146	0.0280	2
125*	2MASX J17132646-2332016	0.0342	2
126*	2MASX J17132844-2308406	0.0280	2
127	2MASX J17132963-2234086	0.0323	2
128*	2MASX J17133402-2337336	0.0252	2
129	2MASX J17133908-2239286	0.0309	2
130*	OPH J171339.33-231814	0.0315	2
131	2MASX J17134226-2353126	0.0297	2
132	2MASX J17135024-2216106	0.0329	3
133	2MASXiJ1713516-240757	0.0258	2
134*	2MASX J17135195-2303286	0.0304	2
135*	2MASX J17135221-2321556	0.0285	2
136*	2MASX J17135490-2316186	0.0330	2
137*	2MASX J17135847-2251566	0.0297	2
138*	2MASX J17140172-2313026	0.0284	2
139*	2MASX J17140971-2331536	0.0293	2
140*	2MASX J17142206-2300182	0.0344	2
141*	2MASX J17142386-2310482	0.0308	2
142*	2MASX J17142479-2313472	0.0262	3
143	2MASX J17143041-2408063	0.0256	2
144	2MASX J17145813-2221299	0.0290	3
145	2MASX J17150845-2354140	0.0303	2
146	2MASX J17150925-2341020	0.0324	2
147	2MASX J17151484-2326579	0.0330	2
148	2MASX J17151503-2301319	0.0285	2
149	2MASX J17154530-2340044	0.0284	2
150	2MASX J17155885-2342043	0.0266	2
151	2MASX J17165090-2324074	0.0286	3
152	2MASX J17181000-2313584	0.0262	3